nature communications

Article

https://doi.org/10.1038/s41467-024-50691-5

Rationally designed Ru catalysts supported on TiN for highly efficient and stable hydrogen evolution in alkaline conditions

Received: 1 March 2024

Accepted: 19 July 2024

Published online: 29 July 2024

Check for updates

Jia Zhao[1,2,3], Ricardo Urrego-Ortiz[4,5], Nan Liao[1,2,3], Federico Calle-Vallejo[5,6] & Jingshan Luo[1,2,3]

Electrocatalysis holds the key to enhancing the efficiency and cost-effectiveness of water splitting devices, thereby contributing to the advancement of hydrogen as a clean, sustainable energy carrier. This study focuses on the rational design of Ru nanoparticle catalysts supported on TiN (Ru NPs/TiN) for the hydrogen evolution reaction in alkaline conditions. The as designed catalysts exhibit a high mass activity of 20 A mg^{-1}_{Ru} at an overpotential of 63 mV and long-term stability, surpassing the present benchmarks for commercial electrolyzers. Structural analysis highlights the effective modification of the Ru nanoparticle properties by the TiN substrate, while density functional theory calculations indicate strong adhesion of Ru particles to TiN substrates and advantageous modulation of hydrogen adsorption energies via particle-support interactions. Finally, we assemble an anion exchange membrane electrolyzer using the Ru NPs/TiN as the hydrogen evolution reaction catalyst, which operates at 5 A cm^{-2} for more than 1000 h with negligible degradation, exceeding the performance requirements for commercial electrolyzers. Our findings contribute to the design of efficient catalysts for water splitting by exploiting particle-support interactions.

Heterogeneous catalysts consisting of precious metals supported on substrates have been the focus of extensive research for applications in energy conversion, chemical synthesis, and the removal of pollutants[1–4]. Solid supports play a crucial role in enhancing catalyst performance in various ways. The high surface area supports increase noble metal dispersion and contribute to the creation of highly undercoordinated surface sites. Additionally, metal-support interactions (MSIs) can modulate the adsorption energies by modifying the electronic and geometric properties of the catalyst[5–8]. Consequently, researchers have dedicated significant attention to designing electrocatalysts using strategies that capitalize on MSIs[9–12].

Due to its high activity, high durability, and, in particular, its platinum-like hydrogen adsorption energy, Ru has emerged as a promising alternative to Pt for the hydrogen evolution reaction (HER). However, further optimization is necessary to achieve suitable hydrogen adsorption energies on Ru nanoparticles (NPs) under alkaline conditions[13–17]. To address this issue, various materials, such as carbonitrides[18–20], oxides[21–23], phosphides[24,25], and sulfides[26,27] have been utilized as supports. Nevertheless, most reported electrocatalysts

[1]Institute of Photoelectronic Thin Film Devices and Technology, State Key Laboratory of Photovoltaic Materials and Cells, Tianjin Key Laboratory of Efficient Solar Energy Utilization, Ministry of Education Engineering Research Center of Thin Film Photoelectronic Technology, Nankai University, Tianjin, China. [2]Frontiers Science Center for New Organic Matter, Nankai University, Tianjin, China. [3]Haihe Laboratory of Sustainable Chemical Transformations, Tianjin, China. [4]Department of Materials Science and Chemical Physics & Institute of Theoretical and Computational Chemistry (IQTC), University of Barcelona, Barcelona, Spain. [5]Nano-Bio Spectroscopy Group and European Theoretical Spectroscopy Facility (ETSF), Department of Advanced Materials and Polymers: Physics, Chemistry and Technology, University of the Basque Country UPV/EHU, Av. Tolosa 72, San Sebastian, Spain. [6]IKERBASQUE, Basque Foundation for Science, Plaza de Euskadi 5, Bilbao, Spain. e-mail: federico.calle@ehu.es; jingshan.luo@nankai.edu.cn

display decent HER performance only at low current densities, such that reaching high performance at the large current densities required for industrial scale operation remains a challenge[28,29]. Moreover, the stable interaction between metal and substrate is one of the prerequisites for catalysts to meet commercial demands. In this order of ideas, identifying a substrate capable of strongly anchoring Ru nanoparticles while properly tuning their electronic structure is highly desirable.

Two important metal-support phenomena, namely charge transfer and strong metal-support interactions (SMSI), have been shown to influence the activity of metal catalysts[30]. Specifically, differences in the Fermi level of metal NPs and supports cause electrons to rearrange at the interface until reaching an equilibrium, inducing changes in the oxidation state of the metal atoms within both materials that ultimately alter their adsorption properties. Therefore, careful consideration of surface properties and electrical conductivity is essential when selecting suitable supports[31–33]. In addition, the strength of the metal-support grip, described by the adhesion energy (Φ_{adh}), plays a critical role in preventing agglomeration and detachment of metal nanoparticles at high current densities. In this regard, the adhesion energy must be considered when selecting the support[3]. Titanium nitride (TiN) exhibits distinct properties such as mechanical hardness, oxidation resistance, and high electrical conductivity (4000 S cm^{-1}), which make it a promising choice for supporting precious metal nanoparticles[34–37]. Zhang et al. attributed the remarkable HER performance of Pt-TiN nanorod arrays in 0.5 M H_2SO_4 to strong metal-substrate interactions between Pt and TiN, which mitigated Pt aggregation[38]. Anandhababu et al. explored Ir-TiN nanowires as bifunctional electrocatalysts in both acidic and neutral media. Density functional theory (DFT) calculations indicated that TiN plays an important role in modulating the adsorption energy of the reaction intermediates[39]. Lee et al. loaded single atomic Pt on a N-vacancy site of a TiN support. TiN effectively anchors Pt atoms, which are active for electrochemical oxygen reduction, formic acid oxidation and methanol oxidation[40]. Additionally, Ti displays pronounced hydrophilicity and can effectively facilitate the dissociation of water during catalytic processes[13,21,41].

Considering all of the above, in this work TiN-supported Ru NPs (hereon Ru NPs/TiN) were prepared via immersion-reduction steps and evaluated as electrocatalysts for the HER. The interaction between TiN and Ru NPs contributes to significant HER performance in alkaline conditions, achieving a current density of −100 mA cm^{-2} at an overpotential of 73 mV. Notably, despite its low Ru content, the normalized mass activity of Ru NPs/TiN is sizably higher than those of commercial Pt/C (20%) and Ru/C (5%). Computational results suggest that the net effect of the TiN support is the weakening of the hydrogen adsorption energies of supported Ru NPs compared to pure Ru surfaces. Such a weakening activates various sites toward the HER. Moreover, DFT calculations also show that Ru NPs have a significantly stronger adhesion to TiN than to graphene. Finally, an anion exchange membrane (AEM) electrolyzer containing the Ru NPs/TiN underwent a continuous operation for more than 1000 h at industrial current densities (1, 2 and 5 A cm^{-2}). Overall, this work presents a viable and cost-effective strategy for the design of advanced electrocatalysts that excel in hydrogen production by harnessing catalyst-support interactions.

Results and discussion

Catalyst synthesis and characterization

The synthesis of the Ru NPs/TiN catalyst is illustrated in Fig. 1a. Firstly, the TiO_2 nanowires were grown on carbon fiber paper (CFP) using a hydrothermal process. The phase structure and morphology (Supplementary Figs. S1 and S2) of the TiO_2 nanowires were characterized by X-ray diffraction (XRD) and scanning electron microscopy (SEM), respectively. Next, an ammonia annealing step was employed to convert TiO_2 into TiN (Supplementary Figs. S3–S5). Finally, the Ru nanoparticles were introduced by an impregnation reduction strategy, which securely anchored the Ru nanoparticles on TiN via strong Ru-N interactions. The XRD pattern of Ru NPs/TiN (Fig. 1j) showed only two sets of peaks. The peaks located at 36.9°, 42.9°, 62.2°, 74.4° and 78.5° are attributed to the (111), (200), (220), (311) and (222) planes of TiN, respectively (PDF#38-1420), while the other peaks are assigned to CFP (PDF#41-1487). No diffraction peaks of Ru can be observed due to the low content of Ru in the catalysts, which was only 0.36 wt%, as identified by inductively coupled plasma optical emission spectrometry (ICP-OES, Supplementary Table S1). The Raman spectrum (Supplementary Figure S6) shows regular TiN peaks without any characteristic peaks belonging to Ru NPs. Field-emission scanning electron microscopy (FESEM, Fig. 1b) shows that introducing Ru NPs does not change the TiN morphology. Figure 1g shows the typical low-magnification high-angle annular dark-field scanning transmission electron microscopy (HAADF-STEM) image of Ru NPs/TiN, which indicates the uniform adherence of the Ru nanoparticles to the substrate, with individual nanoparticles marked by light red circles. The high-magnification HAADF-STEM (Fig. 1h, i) images clearly show the lattice structures, and the measured lattice spacing of 0.211 nm is attributed to the (200) plane of cubic TiN. The hexagonal close-packed (hcp) lattice with a lattice spacing of 0.208 nm is assigned to the (101) plane of the Ru nanoparticles. The scanning TEM coupled with energy dispersive X-ray spectroscopy (STEM-EDX) mappings reveals a homogeneous distribution of Ti, N and Ru (Fig. 1c–f).

X-ray photoelectron spectroscopy (XPS) analysis of Ru NPs/TiN suggests the coexistence of metallic Ru and oxidized Ru (Fig. 2a). In the high-resolution Ti 2*p* XPS spectrum (Figure S7a), Ru NPs/TiN were positively shifted compared to pure TiN, indicating electron transfer from the TiN substrate to the Ru nanoparticles. Compared to TiN, the binding energy of the Ti-N bond in the high-resolution N 1*s* spectrum (Figure S7b) was also positively shifted, further confirming the interaction between TiN and Ru. Moreover, the Ru-N_x bond peak can be clearly observed in the N 1*s* spectrum of Ru NPs/TiN, suggesting strong anchoring of the Ru nanoparticles to the substrate[42]. To gain a deeper understanding of the valence state and coordination environment of Ru in the Ru NPs/TiN, X-ray absorption near edge structure (XANES) and extended X-ray absorption fine structure (EXAFS) measurements were conducted. As shown in Fig. 2b, the K-edge absorption intensity of Ru in Ru NPs/TiN fell between that of RuO_2 and Ru foil, and it was also lower than that of Ru/C. Moreover, compared to the Ru foil, the edge energy of Ru NPs/TiN (Fig. 2c) was shifted to higher energy, but less than that of RuO_2 and Ru/C. In brief, the XANES analysis suggests that the overall valence state of Ru in Ru NPs/TiN lies between that of Ru foil and RuO_2.

The Fourier transforms of the phase-uncorrected EXAFS (Fig. 2d, and Supplementary Fig. S8) show a predominant peak around 1.6 Å for Ru NPs/TiN, matching the Ru−N/O scattering path. The peak positions of Ru-N and Ru-O are indistinguishable[10,13,16–19]. Besides, there is a peak around 2.4 Å for Ru NPs/TiN ascribed to Ru−Ru coordination. The EXAFS fitting curves of Ru NPs/TiN at the Ru k space (Fig. 2d and Supplementary Fig. S9) and the corresponding fitting parameters (Supplementary Table S2) suggest that the coordination numbers of Ru−N/O and Ru−Ru bonds are ~5.7 and 2.4, respectively. Furthermore, the application of EXAFS wavelet transform (WT) analysis provides additional evidence for the coordination environment of Ru in Ru NPs/TiN (Fig. 2g–j).

The work function is one of the most fundamental physical quantities to describe the surface properties of a material. It specifically influences the surface charge distribution of metal-support electrocatalysts and can modify the hydrogen adsorption energy[43,44]. Hence, ultra-violet photoelectron spectroscopy (UPS) was employed to examine the work function and corresponding Fermi level of the prepared materials (Fig. 2e, f). The calculated Φ values are 4.53 and 4.65 eV for TiN and Ru NPs/TiN, respectively. Notably, the Φ value of Ru NPs/TiN is lower than that of pure Ru (4.71 eV). The lower the work function, the more positive the d-band center and the lower the electron binding capacity, which makes it easier for the electron to leave the catalyst surface and participate in the catalytic reaction[45,46].

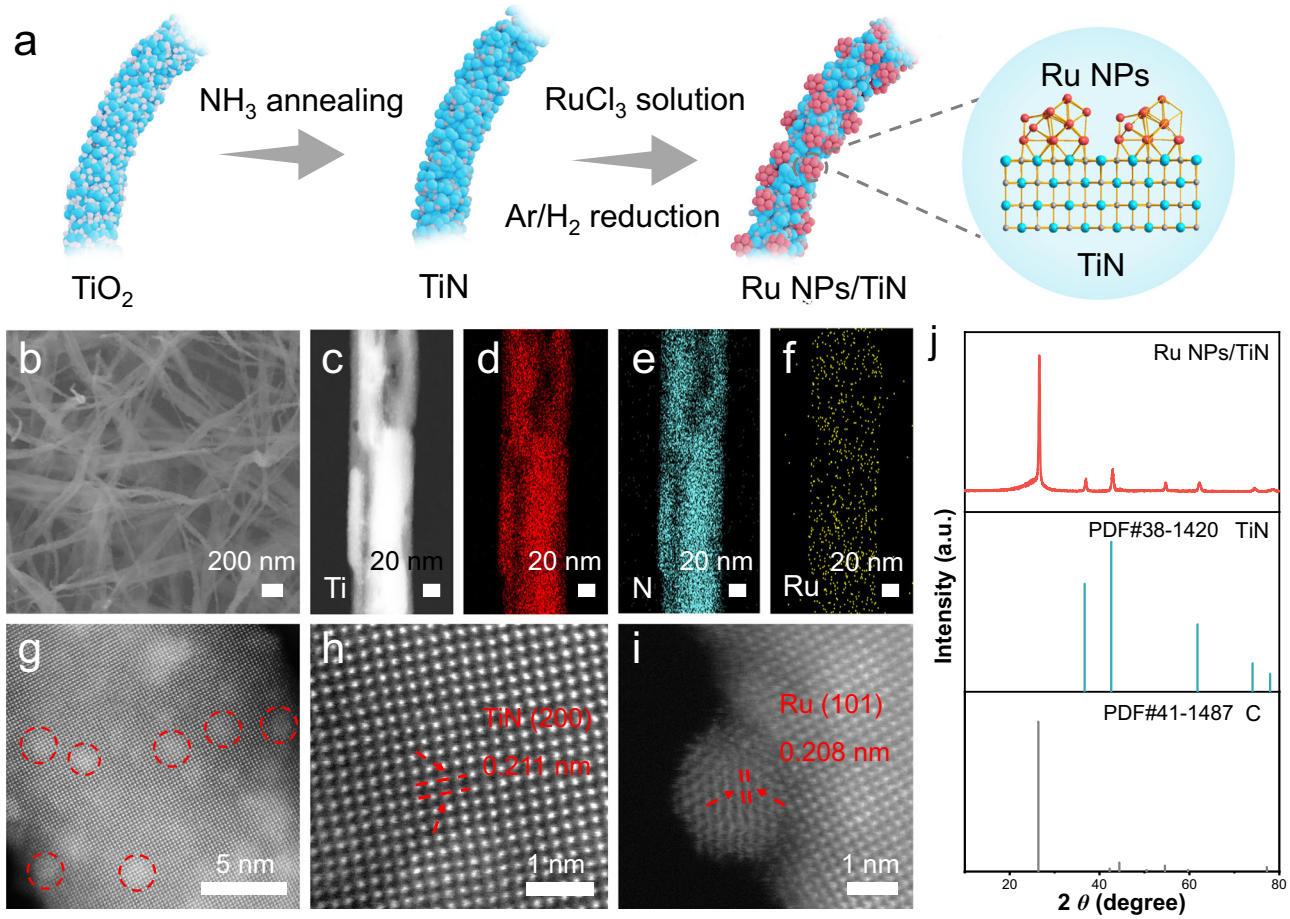

Fig. 1 | Schematics of the synthesis process and characterization of Ru NPs/TiN. a Schematics of the synthesis process for Ru NPs/TiN. **b** SEM image of Ru NPs/TiN. **c**–**f** STEM and corresponding EDS mapping of Ru NPs/TiN. **g**–**i** HAADF–STEM images of Ru NPs/TiN. **j** PXRD pattern of Ru NPs/TiN.

HER performance

To investigate the influence of strong metal-support interactions on the electrocatalytic performance, the HER activities of Ru NPs/TiN, Pt/C, Ru/C, and TiN were evaluated in 1 M KOH. As shown in Fig. 3a, TiN displays the lowest HER activity, necessitating an overpotential of 408 mV at 10 mA cm^{-2}. Upon the introduction of Ru nanoparticles, the HER activity of TiN significantly improves, suggesting that Ru NPs provide the primary active sites for the HER. Specifically, the Ru NPs/TiN electrode displays better HER activity compared to the Pt/C (20%) and Ru/C (5%) benchmarks at the same overpotentials, reaching a current density of −100 mA cm^{-2} at an *iR*-corrected overpotential of 73 mV (*vs* 140 mV for Pt/C and 174 mV for Ru/C). The LSV curves without *iR*–correction are displayed in Supplementary Fig. S10. Furthermore, three additional independent experiments were conducted, and their variances were compared using bar plots (Supplementary Figs. S11a, S12a, and S12b). Potentiostatic measurements (Supplementary Figs. S13, 14) offer insights into the reaction kinetics. The Tafel slope of Ru NPs/TiN (Fig. 3b) is 41.4 mV dec^{-1} at low current densities, significantly lower than those of the benchmark materials and pure TiN substrates (Supplementary Fig. S15), thus aligning with the Volmer-Heyrovsky mechanism. Moreover, the Tafel slope is highly dependent on the surface coverage, relating to both overpotential and rate-determining step (RDS)[47]. Hence, different reaction stages may have different Tafel slope values. The Tafel analysis was performed at different extents of the reaction. Even at high current densities, Ru NPs/TiN maintains the lowest Tafel slope value compared to Pt/C (20%) and Ru/C (5%), further indicating rapid reaction kinetics. The overpotential at 10 mA cm^{-2} and the Tafel slopes at different current densities of the electrocatalysts are summarized in Fig. 3c. For the mass activity of Ru NPs/TiN and the benchmark materials, the current density was normalized by the mass loading of Ru or Pt (Fig. 3d). At an HER overpotential of 63 mV, the mass activity of Ru NPs/TiN is 20 A mg^{-1}_{Ru}, which surpasses the benchmark catalysts and highlights the potential of Ru NPs/TiN for practical applications. The additional three independent experiments determined the error bar for the mass activity (Supplementary Figs. S11b, S12c and S12d). In fact, the mass activity for alkaline HER reported here represents a high performance to date (Fig. 3f, and Supplementary Table S15). In addition, the exchange current density was calculated to be 1.034 mA cm^{-2} for Ru NPs/TiN, outperforming those of commercial Pt/C (1.015 mA cm^{-2}) and Ru/C (1.011 mA cm^{-2}).

Medium-frequency electrochemical impedance spectroscopy (EIS) was employed to characterize the Heyrovsky step, which is one of the charge transfer processes occurring at the electrolyte-catalyst interface. The low charge-transfer resistance of Ru NPs/TiN indicates that it has the fastest electron/proton transfer and the highest HER activity (Figure S16). Furthermore, the kinetic isotope effect (KIE) is a well-established experimental technique for studying reaction kinetics, which involves substituting hydrogen in the electrolytic process for deuterium. Specifically, the difference in reduced mass between the isotopes leads to large differences in reaction rates. The LSV curves of Ru NPs/TiN measured in 1 M KOH/H_2O and 1 M KOD/D_2O are shown in Supplementary Fig. S17, and the calculated KIE for Ru NPs/TiN is 2.2 (Fig. 3e), indicating that the hydrogen produced from water and O-H(D) bond cleavage is the rate-determining step, in accordance with the Tafel analysis. Cyclic voltammetry (CV) curves show clear evidence for the enhanced active area of Ru NPs/TiN compared to pure TiN (Supplementary Fig. S18).

https://doi.org/10.1038/s41467-024-50691-5

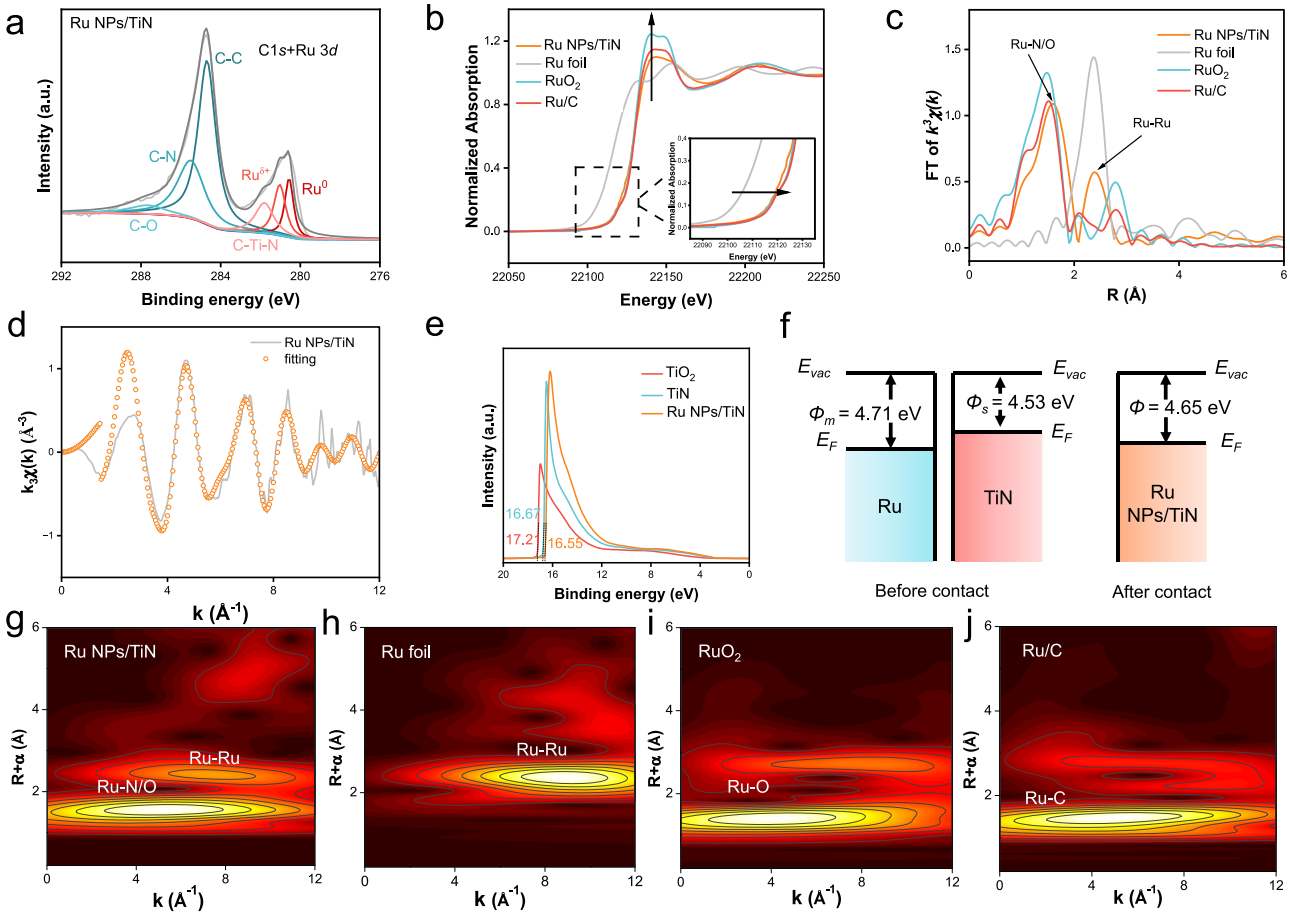

Fig. 2 | XPS and XAS characterizations of Ru NPs/TiN. a High-resolution XPS spectra of C 1*s* and Ru 3*d*. **b** Ru k-edge XANES spectra. **c** The Ru k-edge Fourier transforms of the EXAFS spectra for Ru NPs/TiN, Ru foil, Ru/C, and RuO_2. **d** EXAFS fitting curves of Ru NPs/TiN in the k space. **e** UPS and **f** Fermi level schematic diagram of Ru, TiN and Ru NPs/TiN. **g**–**j** WT-EXAFS curves of Ru NPs/TiN, Ru foil, RuO_2 and Ru/C.

Poisoning experiments were implemented using potassium thiocyanate (KSCN) as the deactivator to verify whether Ru NPs serve as the predominant catalytic sites. SCN^- is capable of adsorbing onto the surfaces of the Ru NPs, inducing a decrease in HER activity. As expected, after introducing 10 mM KSCN into the electrolyte, the potential required to reach 10 mA cm^{-2} increased significantly, which clearly suggests that Ru NPs are the main active sites for HER (Supplementary Fig. S19). To obtain the effective electrochemical active surface area (ECSA), the CV curves were measured in the non-Faradaic region to calculate the double-layer capacitance (C_{dl}), which is proportional to the ECSA (Supplementary Figs. S20 and S21). The Ru NPs/TiN sample displayed the highest C_{dl} among all of the catalysts, which suggests that it contained the largest number of exposed active sites.

A HER catalyst must operate at high current densities and have long-term stability for industrial applications. Ru NPs/TiN displayed a stable HER activity over 1000 h at −1 A cm^{-2} (Fig. 3g). The phase changes after the stability test were investigated by XRD. Supplementary Fig. S22 shows that the diffraction peaks remain essentially unchanged during the test. The TEM image (Supplementary Fig. S23a) shows no obvious changes in the morphology of Ru NPs/TiN after the stability test. The lattice fringes belonging to Ru(101) planes and TiN(200) planes can be clearly observed (Supplementary Fig. S23b). The STEM image and corresponding EDX mappings (Supplementary Figs. S23c–f) indicate the uniform distribution of Ti, N and Ru, showing that there was no Ru leached during the test. XPS was also used to examine the surface properties of the catalyst after experiments. The peak for $Ru^{\delta+}$ disappears (Supplementary Fig. S24a) and only metallic Ru is detected. Prolonged exposure to negative potentials in the test resulted in the reduction of oxidized Ru species. The peak belonging to C-Ti-N is also not detectable after the stability test (Supplementary Fig. S24a). Furthermore, there are no significant differences in Ti 2*p* and N1*s* spectra before and after the stability test (Supplementary Figs. S24b and S24c). ICP-OES was used to detect the metal content before and after stability testing of catalysts and electrolytes and, as indicated in Supplementary Tables S3 and S4, only a small amount of the elements dissolved into the electrolyte. The standard curves for Ru and Ti are shown in Supplementary Fig. S25. Moreover, the LSV curves (Supplementary Fig. S26) before and after the stability test exhibit minimal disparity, providing additional confirmation for the enduring performance of Ru NPs/TiN. In comparison, the HER overpotentials of Pt/C (20%) and Ru/C (5%) increased steadily over the first 10 h (Supplementary Fig. S27). Furthermore, the stability of Ru NPs/TiN was evaluated by measuring multi-potential step curves. When different current densities were applied from −10 to −200 mA cm^{-2} and back to −10 mA cm^{-2}, a negligible change in the potential was observed (Supplementary Fig. S28). Overall, the high activity and durability of Ru NPs/TiN make it a suitable alternative to commercial Pt/C and Ru/C catalysts for industrial HER applications in alkaline conditions.

Computational modeling

We used DFT calculations to shed light into the enhancing effect of the TiN support on the catalytic activity of Ru. Details of the calculations are presented in "methods" section and the structures of the systems that provide the most stable hydrogen adsorption energies are shown in Supplementary Fig. S29. Figure 4a shows the pure, extended Ru surfaces and an exemplary Ru NP supported on TiN(100). In view of the high pH

https://doi.org/10.1038/s41467-024-50691-5

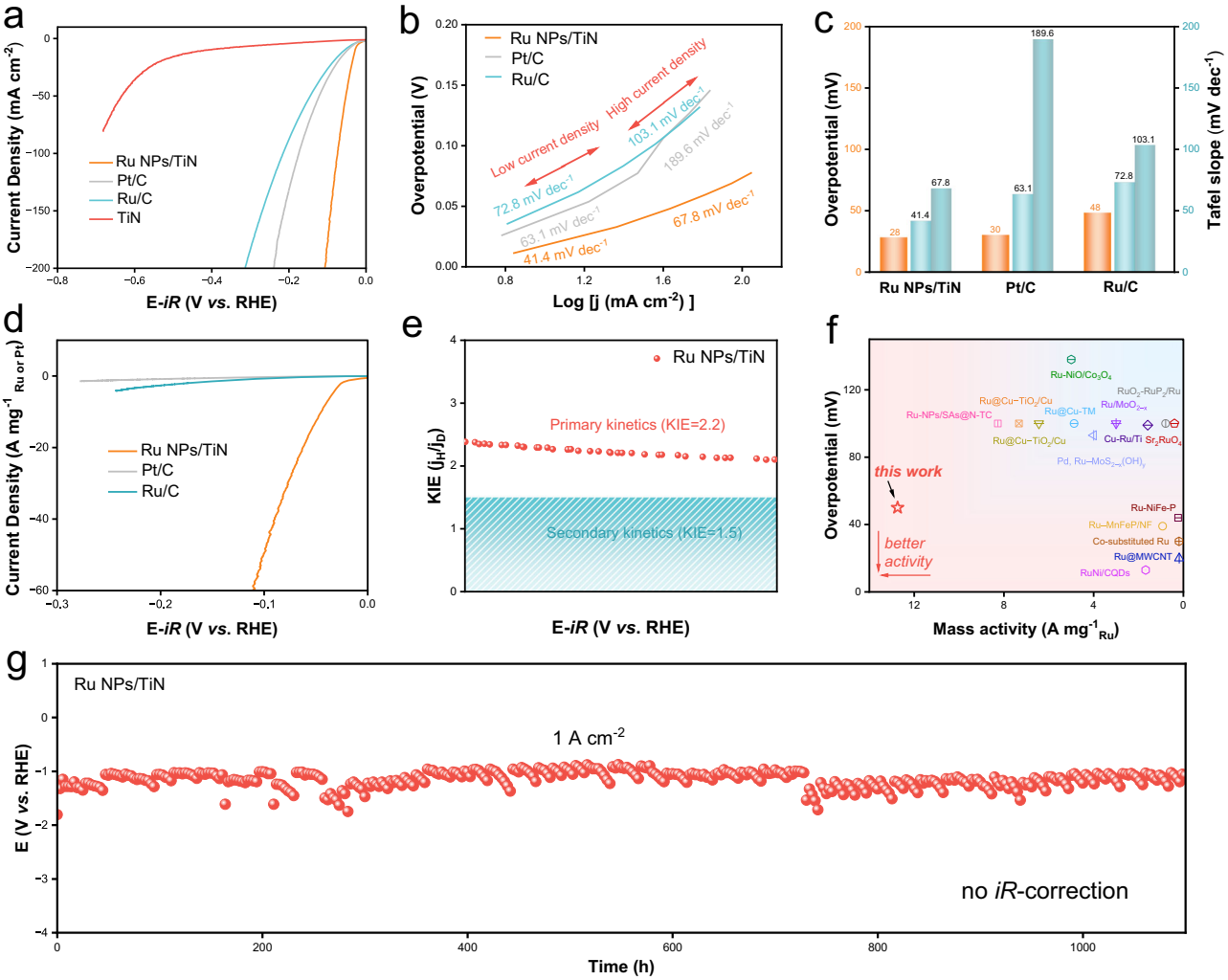

Fig. 3 | Electrochemical performance of Ru NPs/TiN in a three-electrode system. **a** LSV curves of Ru NPs/TiN, Pt/C (20%), Ru/C (5%) and TiN. Geometric area of the electrode: 1 cm^2; electrolyte: 1 M KOH, pH = 13.83; scan rate: 1 mV s^{-1}; temperature: 25 °C. The solution resistances of Ru NPs/TiN, Pt/C (20%), and Ru/C (5%) are 1.74, 2.06, and 2.8 Ω, respectively. **b** Tafel plots of Ru NPs/TiN, Pt/C and Ru/C. **c** Bar plot comparing the overpotential at 10 mA cm^{-2} and the Tafel slope at different current densities. **d** Noble metal content normalized HER LSV curves. **e** KIE test of Ru NPs/TiN. **f** Comparison of the HER activity in alkaline conditions of Ru NPs/TiN and other Ru-based electrocatalysts in the literature (Table S15). **g** Chronopotentiometry measurement of Ru NPs/TiN conducted at 1 A cm^{-2}. Geometric area of the electrode: 1 cm^2; electrolyte: 1 M KOH, pH = 13.83; temperature: 25 °C.

of our experiments, the proton source is H_2O and, thus, hydrogen adsorption (ΔG_H) was calculated using a liquid water reference (Eq. 1). As this reaction corresponds to water dissociation, we analyzed the surface decomposition of water on Ru-containing systems and show their advantages with respect to Pt(111) in Computational Details.

$$H_2O_{(l)} + e^- + * \rightarrow *H + OH^-_{(aq)} \quad (1)$$

To model the HER incorporating particle-support effects, we calculated ΔG_H on various TiN(100)-supported Ru NPs (Ru/TiN) and extended surfaces of Ru. For Ru/TiN, 21 different NPs were constructed with active sites the coordination number (*cn*) of which were in the range of 1 to 9. This ensured at least three different adsorption sites per *cn* (except for *cn* = 9 which proved challenging to sample in reasonably sized clusters). For pure Ru, we considered Ru(105) and Ru(109) surfaces, and hydrogen adsorption was evaluated on sites with *cn* between 7 and 10.33. Supplementary Table S6 and S7 contain the hydrogen adsorption energies (ΔG_H) in Fig. 4 and the coordination number of each active site.

Figure 4b presents the trends in ΔG_H for pure Ru and the supported NPs as a function of *cn*, along with the corresponding linear fits and residual errors (MAE/MAX stand for mean/maximum absolute errors). For pure and TiN(100)-supported Ru, the adsorption energies were averaged for sites with the same *cn*, and in such cases, the standard deviation was used to define the error bars. In Fig. 4b, both Ru/TiN and pure Ru display positive linear trends, indicating that hydrogen adsorption weakens as the coordination of the adsorption sites increases[48–50]. More importantly, the two linear trends have similar slopes (0.10 for Ru/TiN vs 0.09 for pure Ru) and different intercepts: the Ru/TiN trend is above the pure Ru trend by ~0.27 eV. Hence, the net effect of the TiN support is a systematic weakening of hydrogen adsorption. Computational Details show that the trends in ΔG_H on pure and supported Ru are also captured by more elaborate electronic descriptors, such as the *d*-band center (ε_d) and the integrated crystal orbital overlap population (*iCOOP*) integrated to the Fermi level. This analysis was carried out for the sites on Ru NPs with the most stable hydrogen adsorption energies (see Supplementary Fig. S29). Supplementary Figs S31–S34 show that ΔG_H is inversely proportional to those two descriptors, in line with previous works[51]. Furthermore, for both Ru/TiN and pure Ru, ε_d and *iCOOP* display reasonable predictive

https://doi.org/10.1038/s41467-024-50691-5

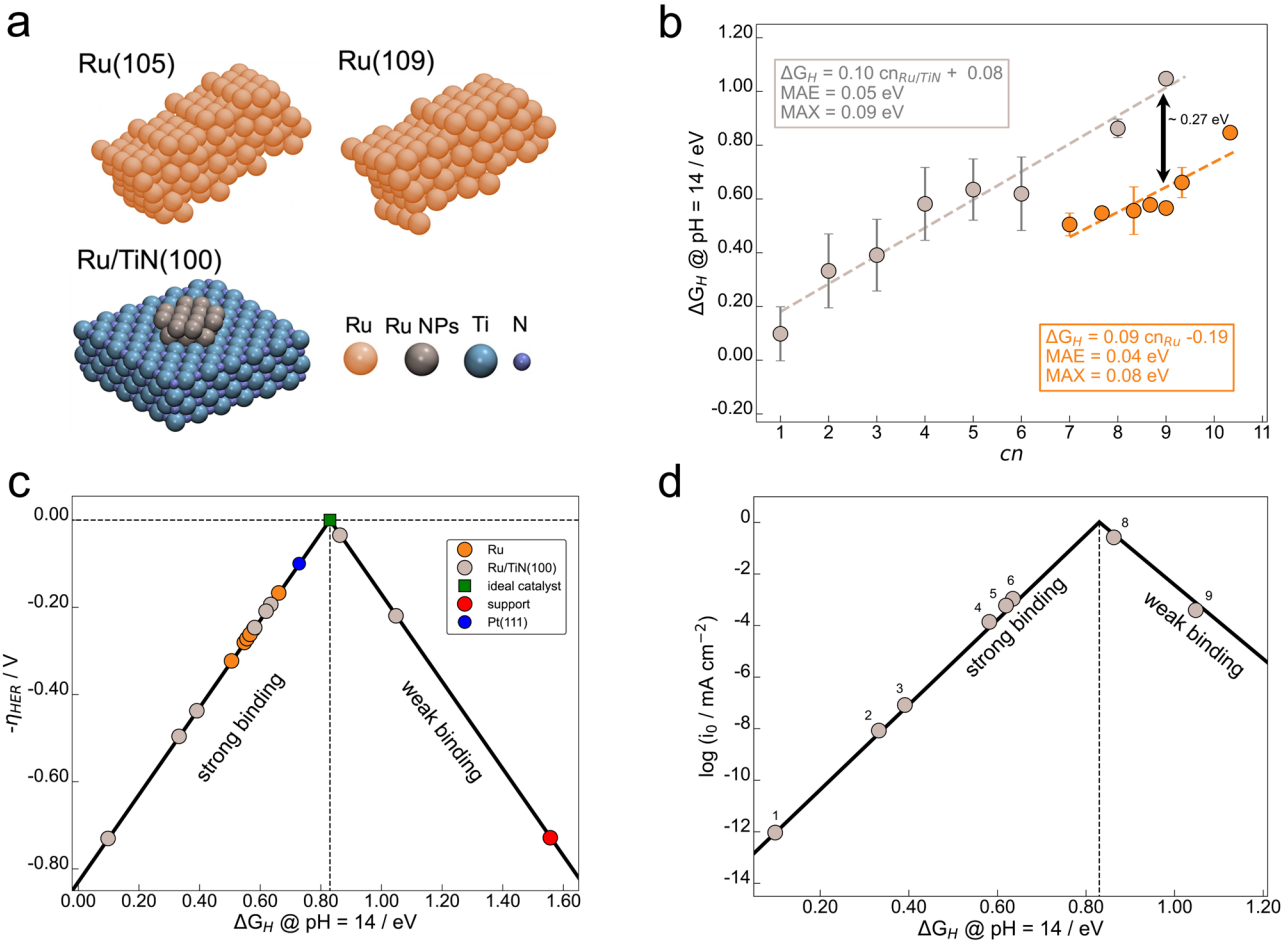

Fig. 4 | DFT investigation of hydrogen adsorption and evolution on Ru/TiN. **a** Schematics of the electrocatalytic systems. Ru(105) and Ru(109) are surface facets of extended Ru. Ru/TiN(100): Ru NPs supported on TiN(100). **b** Relationships between the hydrogen adsorption energies (ΔG_H) and the coordination numbers (*cn*) of sites at Ru NPs (gray) and pure Ru (orange), along with their linear fits. MAE/MAX: mean/maximum absolute errors. The trends in both cases were built using the averages of each *cn*; the error bars span the standard deviation of the averages. As the lines have similar slopes but the intercepts differ by -0.27 eV, the net effect of TiN(100) is the weakening of ΔG_H. **c** Thermodynamic volcano plot of the HER overpotential as a function of ΔG_H for sites on pure and supported Ru. For comparison, we include the ideal catalyst (green), TiN(100) (red), and Pt(111) (blue). **d** HER volcano plot for TiN(100)-supported Ru NPs built upon the experimental exchange current density (i_0) of Ru/TiN(100). The labels show the corresponding *cn* of the Ru NP sites. In (**c**, **d**), sites with *cn* = 8 on supported Ru NPs are closer to the volcano apex than those in pure Ru, indicating enhanced HER activity. In all cases, ΔG_H was calculated at pH = 14.

capabilities. In fact, ε_d and *iCOOP* result in MAE/MAX of 0.13/0.34 eV and 0.16/0.38 eV for Ru/TiN, respectively, and MAE/MAX of 0.01/0.03 eV and 0.02/0.07 eV for pure Ru. Notably, when set side by side with *cn*, the latter offers enhanced predictiveness (MAE/MAX of 0.06/0.16 eV for the NP sites producing the most stable adsorption energies for each *cn* in Fig. 4b, see Supplementary Fig. S30) without requiring self-consistent calculations.

To assess the effect of the TiN support on the HER activity of Ru sites, we built the thermodynamic Sabatier-type activity plot in Fig. 4c[52]. In this case, the activity is expressed as the additive inverse of the HER overpotential ($-\eta_{HER}$). In this plot, $-\eta_{HER} = 0$ is the top of the volcano and corresponds to $\Delta G_H = 0.83eV$. This optimal adsorption energy is attained by the HER ideal catalyst, depicted in green. Furthermore, the volcano shows that all the pure Ru sites under study concentrate on the strong-binding (left) region, displaying η_{HER} values between 0.32 and 0.17 V. Conversely, TiN-supported Ru NPs produce a wider range of adsorption energies from 0.1 to 1.05 eV, which cover both sides of the activity plot. Interestingly, there is a nearly optimal active site with $\eta_{HER} = 0.03V$. The volcano plot also includes pristine TiN, which performs poorly as HER catalyst in view of its weak hydrogen binding ($\Delta G_H = 1.56eV$ producing a $-\eta_{HER}$ as large as −0.73 V; see also a comparison with previous reported data in Computational Details, and Pt(111), which binds *H ~ 0.1 eV more strongly than the optimal catalyst, set at −0.83 eV. Figure 4c shows that the active centers of Ru NPs with *cn* = 8 are more active than Pt(111) in terms of thermodynamic overpotential.

To supplement the thermodynamic viewpoint, Fig. 4d connects the exchange current density to the DFT-calculated adsorption energies of the Ru NPs through an affordable microkinetic model (full details are provided in "Methods" section)[52]. As the adsorption energies of the Ru NPs are related to *cn* following Fig. 4b, this semiempirical model also enables a connection between the reaction kinetics and the structure of the catalyst. In fact, the labels in Fig. 4d indicate the respective *cn* of each TiN-supported Ru NP site, and shows that adsorption centers with *cn* close to 8 and metal-support interactions display the highest current densities.

Finally, DFT was used to assess the stability of the Ru NPs supported on TiN and C, see Figures S35 and S36 and Table S11. A Ru particle composed of 17 atoms bound to TiN(100) and graphene yields total adhesion energies of −20.42 and −2.99 eV, respectively. This sizable difference is in line with the experimental observation that the stability of Ru/TiN is higher than that of Ru/C. When accounting for the number of Ru atoms in direct contact with TiN(100) and graphene (7 in both cases), the adhesion energies per atom are −2.92 and −0.43 eV/atom,

https://doi.org/10.1038/s41467-024-50691-5

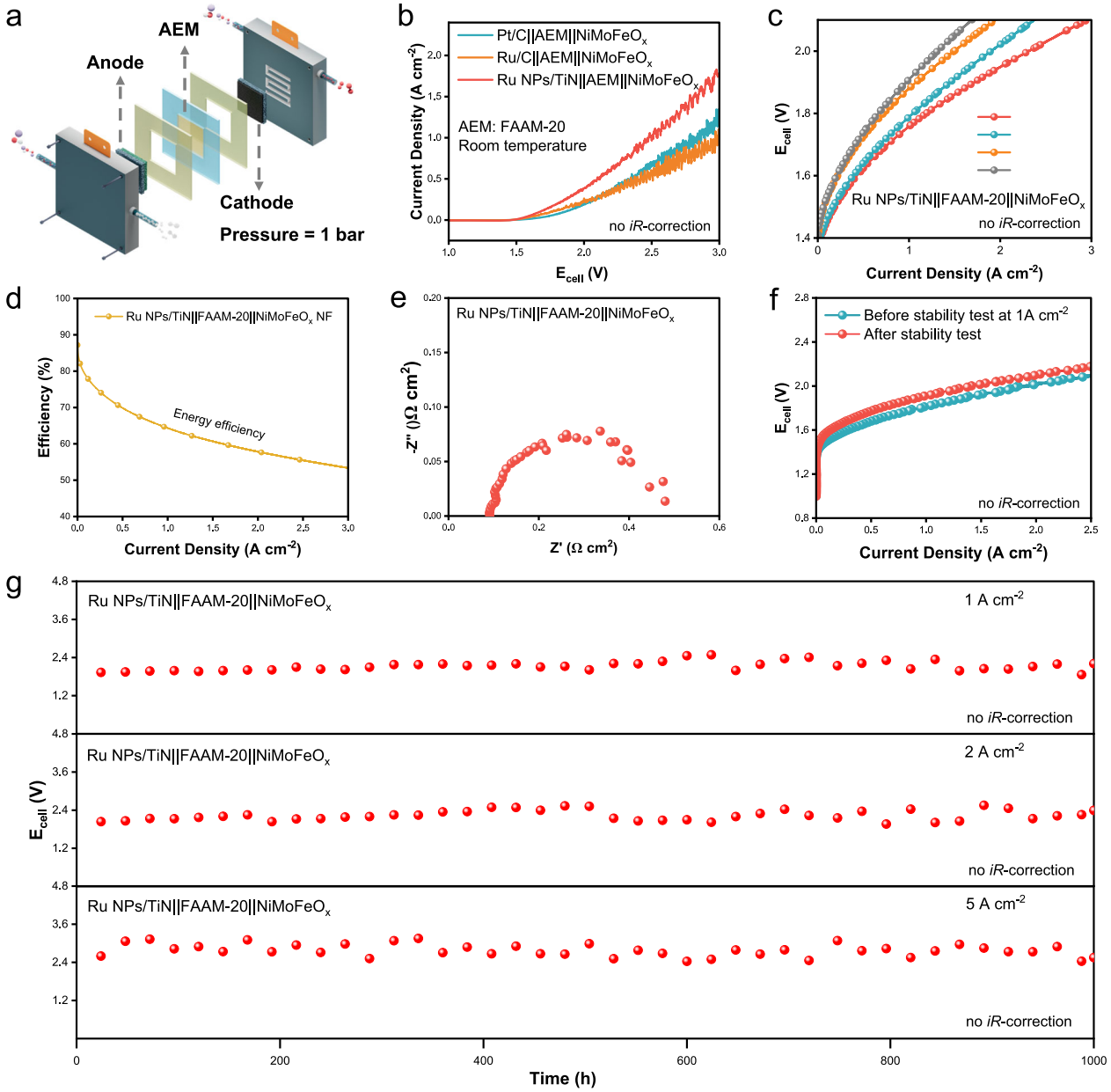

Fig. 5 | Electrochemical performance of Ru NPs/TiN in AEM electrolyzers. **a** Schematics of the AEM electrolyzer. **b** J–V curves of the AEM electrolyzer using Ru NPs/TiN, commercial Pt/C (20%) and Ru/C (5%) as the cathode catalyst and NiMoFeO$_x$ NF as the anode catalyst, measured at 25 °C and 1 bar. Geometric area of the electrode: 1 cm^2; electrolyte: 30% KOH; scan rate: 1 mV s^{-1}. **c** LSV curves of the Ru NPs/TiN | |FAAM-20 | |NiMoFeO$_x$ NF AEM electrolyzer measured at different temperatures. Geometric area of the electrode: 1 cm^2; electrolyte: 30% KOH; scan rate: 1 mV s^{-1}. **d** Energy efficiency of Ru NPs/TiN | |FAAM-20 | |NiMoFeO$_x$ NF AEM electrolyzer under different current densities. **e** EIS of the AEM electrolyzer (R_s: 89 ± 3.92 mΩ, 89 is the average of the values of four tests, and 3.92 is the standard deviation). **f** Polarization curves of Ru NPs/TiN | |FAAM-20 | |NiMoFeO$_x$ NF in the AEM electrolyzer measured before and after the stability test. **g** Chronopotentiometry test of Ru NPs/TiN | |FAAM-20 | |NiMoFeO$_x$ NF at 1, 2 and 5 A cm^{-2} in the AEM electrolyzer, measured at 80 °C and ambient pressure. Geometric area of the electrode: 1 cm^2; electrolyte: 30% KOH.

respectively. Furthermore, additional calculations of the per-atom binding energies of Ru_{17} bound to graphene with one (−1.52 eV/atom) and two vacancies (−2.25 eV/atom) suggest that only when numerous defects are created, may the adhesion energies of a given Ru cluster on graphene approach that on TiN(100) (see Supplementary Table S11 and Supplementary Figure S36). Further details on the stability calculations can be found in "methods" section. The optimized coordinates of all of the modeled systems can be found in the supplementary data 1.

AEM electrolyzer performance

In pursuit of optimal electrolytic cell performance, various oxygen evolution reaction (OER) electrocatalysts were developed, which also play an important role during water splitting. As depicted in Supplementary Figs. S37–S38, NiFe layered double hydroxides (NiFe LDH) and NiMoFeO$_x$ were uniformly dispersed on a nickel foam (NF). NiMoFeO$_x$ has a better OER performance than traditional NiFe LDH (Supplementary Fig. S39) and can operate stably at a current density of 200 mA cm^{-2} (Supplementary Fig. S40). Subsequently, we assembled an AEM electrolyzer using Ru NPs/TiN and NiMoFeO$_x$ NF as the HER and OER electrocatalysts, respectively, to assess the practical application potential of the electrocatalysts under industrial operating conditions. The electrolyzer cell, schematically illustrated in Fig. 5a, featuring the NiMoFeO$_x$ NF anode and Ru NPs/TiN cathode, was operated at 80 °C and 1 bar, with a 30% KOH electrolyte and Fumasep

FAAM-20 as the anion exchange membrane. Supplementary Fig. S41 displays a photograph of the AEM test setup. The characteristic polarization curves without *iR* compensation in Fig. 5b clearly indicate that the electrolyzer with Ru NPs/TiN catalyst has enhanced water electrolysis efficiency at room temperature compared with the commercial Ru/C and Pt/C electrocatalysts, as the former reaches larger current densities at the same cell potentials compared to the latter.

Figure 5c displays the polarization curves of the Ru NPs/TiN | | FAAM-20 | |$NiMoFeO_x$ NF electrolyzer tested under different temperatures. The results indicate that the reaction temperature has a substantial influence on the performance. Specifically, these values correspond to energy efficiencies (neglecting the thermal energy input and calculated using Equations S1 and S2) of 70.1, 64.3 and 58.0%, respectively (Fig. 5d). Three additional independent LSV tests were conducted, and the corresponding energy efficiencies are given in Supplementary Figs. S42 and S43, which exhibit no significant differences in performance (Supplementary Tables S13 and S14). By means of EIS, we evaluated the ohmic resistance (R_s) and charge-transfer resistance (R_{ct}). We found negligible R_s and R_{ct} for the AEM cell, as depicted in Fig. 5e. Moreover, R_s (89 ± 3.92 mΩ) remains consistent across four independent tests, with minor variations observed in R_{ct} (Supplementary Figs. S44 and S45).

A long-term chronopotentiometry test of the Ru NPs/TiN | |FAAM-20 | |$NiMoFeO_x$ NF electrolyzer was also performed to evaluate its long-term operation stability for alkaline electrolysis. Figure 5 g shows that the voltage of the Ru NPs/TiN | |FAAM-20 | |$NiMoFeO_x$ NF electrolyzer does not change significantly at current densities of 1.0, 2.0 and 5.0 A cm^{-2} over 1000 h of continuous operation, validating the stability of the electrolyzer under fixed galvanostatic conditions with ampere-level current densities. The curve experiences fluctuations due to gas bubble formation, growth, and desorption. The addition of fresh electrolyte is yet another source of fluctuations. In addition, no obvious degradation in performance was observed from the polarization curves after conducting the stability test at 1 A cm^{-2} (Fig. 5f). In terms of both performance and stability, the Ru NPs/TiN | |FAAM-20 | |$NiMoFeO_x$ NF electrolyzer exhibits clear advantages compared to AEM cells in the literature (Supplementary Table S16). In brief, the low cell potential and long stability of the Ru NPs/TiN | |FAAM-20 | |$NiMoFeO_x$ NF electrolyzer evidence its potential for industrial application.

In summary, a highly active Ru NPs/TiN HER electrocatalyst was designed and synthesized via a facile and cost-effective method. The Ru NPs are homogeneously dispersed on the TiN supports and there is catalyst-support charge transfer. HER measurements in alkaline conditions showed an overpotential as low as 73 mV at −100 mA cm^{-2} for Ru NPs/TiN. Notably, the normalized mass activity of Ru NPs/TiN is higher than those of commercial Pt/C (20%) and Ru/C (5%). Structure-sensitive analyses and Sabatier-type volcano plots built upon DFT calculations showed that the TiN support weakens hydrogen adsorption on Ru NPs with respect to extended Ru electrodes. Because pure Ru binds hydrogen too strongly, such a weakening enhances the catalytic performance. In addition, computational results also showed that Ru NPs adhere more strongly to the TiN support compared to a C-based support. Moreover, due to the strong metal-support interactions, Ru NPs/TiN are able to deliver more than 1000 h of stable operation at ampere-level (1, 2 and 5 A cm^{-2}) water-splitting current densities in an AEM electrolyzer. These findings illustrate the effectiveness of metal-support interactions in enhancing the overall catalytic performance of Ru NPs and highlight their potential for practical implementation in large-scale green H_2 generation using AEM cells.

Methods

Chemicals

Ruthenium chloride hydrate ($RuCl_3 \cdot H_2O$, 98%) and tetrabutyl titanate ($C_{16}H_{36}O_4Ti$, 98%) were purchased from Macklin. Nickel nitrate hexahydrate [$Ni(NO_3)_2 \cdot 6H_2O$] (99%), iron nitrate nonahydrate [$Fe(NO_3)_2 \cdot 9H_2O$] (99%) and sodium molybdate dihydrate [$Na_2MoO_4 \cdot 2H_2O$] (99%) were purchased from Aladdin. Pt/C (20%, normally 20% Pt on carbon black) and Ru/C (5% Ru on carbon black) were purchased from Alfa Aesar. Acetone (analytically pure) and hydrochloric acid (HCl, 36%) were purchased from Tianjin Chemical Reagent Co., Ltd. Carbon fiber paper and Ni foam (2 mm thickness) were purchased from Suzhou JiaShiDe Foam Metal Co., Ltd. All chemicals were used without further purification. CFP was pretreated in a plasma cleaner before use. NF was cleaned with 1 M HCl and distilled water, and dried in a vacuum drying oven before use. Fumasep FAAM-20 anion exchange membrane was purchased from SCI Materials Hub.

Characterizations

A Panalytical diffractometer (the Netherlands) (40 kV, 15 mA, 600 W) was used for X-ray diffractometry (XRD) at room temperature. Scanning electron microscopy images were tested by a field-emission scanning electron microscope (JSM-7800F, Jeol, Japan). Transmission electron microscopy, high-resolution transmission electron microscopy, and energy-dispersive X-ray spectroscopy were tested by a transmission electron microscopy microscope (JEM-2800, Jeol, Japan). HAADF-STEM images were tested by aberration-corrected transmission electron microscope (JEM-ARM200F). X-ray photoelectron spectrometer (Thermo Scientific ESCALAB 250Xi, USA) with Al Kα (hν = 1486.6 eV) radiation was performed to detect the valence states of the elements, using the carbon peak as a reference to calibrate binding energies[53]. Inductively coupled plasma optical emission spectroscopy was conducted on Agilent 5110 (pump rate :100 r min^{-1}, plasma gas: 12.0 L min^{-1}; nebulizer flow :0.70 L min^{-1}; stable time: 20 s; auxiliary gas: 1.0 L min^{-1}; reading access time: 5 s; sample flush time: 20 s; RF power: 1150 W). Raman spectra were measured on a JMS1000 (Edinburgh instruments, laser: 532-nm). The pH was tested by pH meter (Mettler Toledo, FiveEasy plus, FE28).

Synthesis of CFP supported TiN

Before the experiments, the CFP (3×3 cm^2) was pretreated in a plasma cleaning instrument. Firstly, TiO_2 nanowires were grown on the CFP using a hydrothermal method. The CFP was immersed in a $C_{16}H_{36}O_4Ti$ ethanol solution (obtained by dissolving 0.32 g $C_{16}H_{36}O_4Ti$ in 20.0 mL anhydrous ethanol), ultrasonicated for 40 min, then annealed in a muffle furnace at 400 °C for 30 min. This formed the TiO_2 seeds on the surface of the CFP. Next, 15 mL HCl, 15 mL acetone, and 1.5 mL $C_{16}H_{36}O_4Ti$ were added into a Teflon-lined stainless autoclave (50 mL volume) and the CFP coated with TiO_2 seeds was dipped into the solution. The hydrothermal reaction was maintained at a constant temperature of 200 °C for 80 min in an electric oven and then cooled at room temperature. The sample was then sonicated with deionized water for 10 min and dried in a vacuum oven at 60 °C for 6 h. This process covered the entire surface of the CFP with a uniform white film of TiO_2 nanowires. Finally, the samples were annealed in NH_3 at 900 °C for 3 h with a heating rate of 3 °C min^{-1} to produce the CFP supported TiN.

Synthesis of CFP supported Ru NPs/TiN

The CFP supported TiN was immersed in 5 mL 20 mg mL^{-1} $RuCl_3 \cdot H_2O$ aqueous solution and stirred for 24 h, then annealed in a tube furnace at 500 °C for 2 h at a heating rate of 3 °C min^{-1} under an Ar/H_2 atmosphere to obtain CFP supported Ru NPs/TiN.

Synthesis of NiFe LDH/NF

The NiFe LDH/Ni foam electrodes were prepared via a hydrothermal growth method with a slightly adjusted protocol. Specifically, 0.15 g of $Ni(NO_3)_2$, 0.20 g of $Fe(NO_3)_3$, and 0.3 g of urea were dissolved in 36 mL of deionized water. Once dissolved, the solution was transferred into a 50 mL autoclave containing a piece of Ni foam positioned against the wall. The hydrothermal synthesis was conducted at 120 °C in an electric oven for 6 hours. Subsequently, the autoclave was allowed to cool

naturally to room temperature, and the samples were then retrieved, rinsed with deionized water, and air-dried under ambient conditions[53].

Synthesis of NiMoFeOx/NF

Firstly, the commercial NF was washed with 1 M HCl and distilled water. Next, one piece of NF (3 $cm^2 \times 3$ cm^2) was immersed in 30 mL H_2O containing $Ni(NO_3)_2{\cdot}6H_2O$ (0.04 M), $Fe(NO_3)_2{\cdot}9H_2O$ (0.02 M) and $Na_2MoO_4{\cdot}2H_2O$ (0.01 M) in a 50 mL autoclave, then reacted at 150 °C in an electric oven for 6 h. After allowing the autoclave to cool naturally to room temperature, the samples were removed, washed with deionized water, and dried naturally in ambient conditions.

Electrochemical measurements using a three-electrode system

All electrochemical measurements were performed using a conventional three-electrode configuration on a CHI 760E electrochemical workstation (CHI Instruments, China). A platinum electrode and a Hg/HgO electrode were used as the counter electrode and reference electrode, respectively. The method for preparing 1 M KOH is as follows: Dissolve 28 grams of potassium hydroxide in 500 mL of water with ultrasound assistance until fully dissolved. Store the solution in a polytetrafluoroethylene container. The CFP supported Ru NPs/TiN was used as the working electrode, and the geometric area was 1 cm^2. Linear sweep voltammetry (LSV) was performed at a rate of 1 mV s^{-1} in 1 M KOH. Cyclic voltammetry (CV) was conducted at a rate of 10 to 50 mV s^{-1} to calculate the double layer capacitance (C_{dl}). The potential *vs*. Hg/HgO was converted to the potential *vs*. the reversible hydrogen electrode (RHE) according to the equation: $E_{RHE} = E_{Hg/HgO} + 0.098 + 0.0592\,pH$. The pH of the electrolyte was 13.83 ± 0.05, as measured by the pH meter. The pH meter was calibrated using buffer solutions of various pH levels (potassium hydrogen phthalate solution, pH = 4.00; mixed phosphate solution, pH = 6.86; sodium tetraborate solution, pH = 9.18) before being used. The process: (1) the electrode was rinsed with deionized water and excess drops were gently blotted with a lint-free tissue. (2) The electrode was placed into the first buffer, so the electrode tip and junction were fully immersed in the buffer. (3) We pushed the calibrate button and waited for the reading to stabilize. (4) We repeated the above steps until all three calibrations were complete, then pushed the reading button. (5) The electrode was rinsed with deionized water and excess drops were gently blotted with a lint-free tissue. (6) We placed the electrode into the 1 M KOH solution, the electrode tip and junction being fully immersed in the solution. (7) We pushed the reading button until the reading stabilized and recorded the pH. All polarization curves were *iR* corrected. The solution resistance (R_s) was tested by potentiostatic electrochemical impedance spectroscopy (EIS) at frequencies ranging from 0.01 Hz to 100 kHz with an AC signal amplitude of 5 mV. Stability was examined by chronopotentiometry testing at −10, −50, −100 and −1 A cm^{-2}. The electrocatalyst inks of Pt/C (20%) and Ru/C (5%) were prepared by mixing them (2.1 mg) with a solution containing a ratio of 10 (100 µL):10 (100 µL):1 (10 µL) of water to ethanol and Nafion binder, respectively. Subsequently, the ink (100 µL) was deposited onto one side of a 1 cm x 1 cm carbon paper substrate and allowed to dry in air. The mass loading of both electrocatalysts was maintained at 1 mg cm^{-2}. ICP-OES was utilized for detecting the metal content before and after the stability testing of catalysts and electrolyte. The formulas used are indicated in Eqs. 2 and 3:

$$C_x\left(\frac{mg}{kg}\right) = \frac{C_0\left(\frac{mg}{L}\right) * f * V_0\,(mL) * 10^{-3}}{m(g) * 10^{-3}} = \frac{C_1\left(\frac{mg}{L}\right) * V_0(mL) * 10^{-3}}{m(g) * 10^{-3}} \tag{2}$$

$$W(\%) = \frac{C_x\left(\frac{mg}{kg}\right)}{10^6} \times 100\% \tag{3}$$

The formula for the electrolyte concentration is indicated in Eq. 4:

$$C_1\left(\frac{mg}{L}\right) = C_0\left(\frac{mg}{L}\right) * f * V_0(mL)/V(mL) \tag{4}$$

m: quality of samples; V_0: constant volume of samples; C_O: concentration of test solution elements, in units of mg L^{-1}; C_I: concentration of elements in the original solution of the sample digestion solution, in units of mg L^{-1}. C_x: final test result of the measured element; f: dilution factor; W (%): final test result of the measured element, expressed as a percentage.

AEM electrolyzer testing

The AEM electrolyzers employed a zero-gap electrolysis cell made from stainless steel, featuring corrosion-resistant anode and cathode flow field plates, Ni foam gas diffusion layers (both in cathode and anode), and Teflon gasketing. The cathode options included Ru NPs/TiN, Pt/C (20%), and Ru/C (5%), while the anode choices were $NiMoFeO_x$/Ni foam and NiFe LDH/Ni foam. Both cathode and anode had a geometric area of 1 cm^2. The Pt/C (20%) and Ru/C (5%) had a mass loading of 1 mg cm^{-2}, consistent with the three-electrode system. To prepare 30% KOH, 150 grams of KOH were dissolved in 350 mL of water using ultrasound until fully dissolved, and the solution was stored in a polytetrafluoroethylene container. Fumasep FAAM-20, with a thickness of 18–22 µm, served as the anion exchange membrane. The membranes, cut into 2.5 cm × 2.5 cm squares, underwent pretreatment in a 6 M aqueous KOH solution for 24 hours at room temperature. To prevent CO_2 contamination and subsequent carbonate formation that could affect conductivity, sealed plastic boxes were used as containers. The membranes were fully submerged in the KOH solution during pretreatment. Specific membrane parameters are detailed in Table S12. A peristaltic pump (Kamoer) delivered 30 wt% KOH electrolyte continuously to the anodic and cathodic half-cells at a flow rate of 30 mL min^{-1} respectively, maintaining a temperature of 80 °C. Electrochemical measurements including LSV and EIS were conducted using a Donghua 4600 electrochemical workstation, with an LSV scan rate of 1 mV s^{-1}. Henghui potential was applied for chronopotentiometry tests. The potentiostat software captured data at one-second intervals. During each current step, the cell voltage was measured to plot points on the polarization curve. Cell resistance was evaluated via EIS measurements conducted under potentiostatic conditions (1.6 V) at 80 °C. Frequency was swept from 100 kHz to 0.01 Hz using an AC signal amplitude of 5 mV. The durability of the AEM electrolyzer was evaluated using chronopotentiometry (CP) measurements, maintaining fixed current densities of 1, 2 and 5 A cm^{-2}.

The energy efficiency of the AEM was calculated as per Eq. 5.

$$\text{Voltage efficiency} = \frac{Thermodynamic\ voltage\,(V)}{Operating\ voltage\,(V)} \tag{5}$$

The thermodynamic voltage, which represents the ideal voltage for water splitting under our operating conditions (80 °C, 1 bar), can be estimated using the following equations[54]:

$$\text{Thermodynamic voltage(V)} = 1.4736 - 0.8212 \times 10^{-3} \times T\,(T\ is\ expressed\ in\ K) \tag{6}$$

Under the conditions of 80 °C and 1 bar, the thermodynamic voltage is computed to be 1.184 V.

Computational details

DFT settings. All DFT calculations were performed using the VASP code and the projector augmented wave (PAW) method to describe the interactions between the valence electrons and the ionic cores[55,56]. In all cases, the PBE exchange-correlation function was employed[57].

The Ru(105) surface cell comprises two (0001) facets, each of them being three atoms long, separated by triangular and square steps, and has a width of two atoms. The Ru(109) surface was composed of five-atoms long (0001) surfaces delimited by triangular and square edges, and a terrace width of two atoms. Both Ru slabs contained five atomic layers. TiN was modeled in its (100) facet using four (6 × 6) atomic layers. Graphene was modeled in its characteristic honeycomb lattice with 72 atoms (6 × 12). A vacuum layer of at least 10 Å was added between the periodic images of all surface slabs in the z direction.

For all surfaces, the atom relaxations were carried out using the conjugate gradient algorithm and, except for graphene, the two bottom layers were kept at the bulk geometry while the upper layers were allowed to move until all the forces between the atoms were below 0.05 eV Å^{-1}. For graphene, all the atoms were allowed to move during the relaxation. The molecules were modeled in 15 Å × 15 Å × 15 Å boxes and the atoms were relaxed in all directions until the forces between them were 0.01 eV Å^{-1} or less.

For the slabs, the Fermi level was smeared using the Methfessel-Paxton method[58] with an electronic temperature of 0.2 eV, while for the molecules a value of 0.001 eV was used. All energies were extrapolated to 0 K. The reciprocal space was sampled using Monkhorst-Pack meshes[59] of (3 × 3 × 1) for TiN, (5 × 3 × 1) for Ru(105), (6 × 2 × 1) for Ru(109), (2 × 2 × 1) for graphene, and only the Γ-point for the molecules. The calculations of the Ru nanoparticles (NPs) supported on TiN (referred to as Ru/TiN) used the same settings of TiN. A plane-wave energy cutoff of 450 eV was used in all calculations.

DFT calculations

Modeled systems. 21 different Ru NPs were built on a TiN(100) surface to adsorb hydrogen on sites with coordination numbers (cn) in the range of 1–9, see the structure of the systems that resulted in the most stable adsorption energies in Figure S29.

Assessment of free energies

The DFT-calculated free energy of a reaction i (ΔG_i^{DFT}) at a pH = 0 with no external potential applied can be approximated as:

$$\Delta G_i^{DFT} \approx \Delta E0_i^{DFT} + \Delta ZPE_i + \Delta \int_0^{298.15K} C_{p,i} dT - T\Delta_i S \quad (7)$$

where $E0_i^{DFT}$ is the ground-state energy, ZPE_i is the zero-point energy calculated within the harmonic oscillator approximation, $\int_0^{298.15K} C_{p,i} dT$ is the integrated heat capacity between 0 and 298.15 K, TS is the product of temperature and entropy, and "Δ" represents the difference between the products and reactants. For the molecules, S can be obtained from thermodynamic tables[60], while for adsorbates it is customary to account for the vibrational contribution only, computed from the vibrational frequencies. Table S5 summarizes the ZPE and TS values in this work.

Free energies of adsorption in acid and alkaline conditions

The adsorption of hydrogen in acidic media is:

$$H^+ + e^- + * \rightarrow *H \quad (8)$$

where $H^+ + e^-$ is a solvated proton-electron pair, * is a free catalytic site, and *H represents adsorbed hydrogen. The free energy of the proton-electron pair is equal to half the free energy of H_2, as defined by the computational hydrogen electrode (CHE)[61]. Thus, $G_{H^+ + e^-}^{DFT} = \frac{1}{2} G_{H_2}^{DFT}$. Using the definition in Eq. 7, ΔG_H^{acid} is calculated as:

$$\Delta G_H^{acid} = \Delta G_{*H}^{DFT} - \frac{1}{2} \Delta G_{H_2}^{DFT} - \Delta G_*^{DFT} \quad (9)$$

We note that $\Delta \int_0^{298.15K} Cp_i dT$ is not included in Equation 9 as the difference between the integral heat capacities of H_2 and *H is below 0.1 eV in the range of 0–298.15 K, and the integrated heat capacity of the catalyst with and without such a small adsorbate is expected to be similar[62,63].

The hydrogen adsorption energy at a pH other than 0 can be calculated as:

$$\Delta G_H^{alkaline} = \Delta G_H^{acid} + 0.059\, pH \quad (10)$$

Alternatively, alkaline hydrogen adsorption can be written as:

$$H_2O_{(l)} + e^- + * \rightarrow *H + OH^-_{(aq)} \quad (11)$$

In this case, Eq. 7 yields:

$$\Delta G_H^{alkaline} = \Delta G_{*H}^{DFT} + \Delta G_{OH^-_{(aq)}}^{DFT} - \Delta G_{H_2O_{(l)}}^{DFT} - \Delta G_*^{DFT} \quad (12)$$

with $\Delta G_{H_2O_{(l)}}^{DFT} = \Delta G_{H_2O_{(g)}}^{DFT} - \Delta_{vap} G_{H_2O}^{exp}$, and $\Delta_{vap} G_{H_2O}^{exp}$ having an experimental value of 0.09 eV[60]. By combining Equations 9, 10 and 12, $\Delta G_{OH^-_{(aq)}}^{DFT}$ can be estimated through the energies of gaseous water and hydrogen (see Eq. 13), avoiding the challenging calculations of aqueous systems using DFT[64,65].

$$\Delta G_{OH^-_{(aq)}}^{DFT} = (\Delta G_{H_2O_{(g)}}^{DFT} - 0.09\, eV) - \frac{1}{2} \Delta G_{H_2}^{DFT} + 0.059 pH \quad (13)$$

We computed the difference between RPBE and PBE hydrogen adsorption energies on Ru(0001) and Pt(111) to allow a direct comparison with the work of Nørskov et al. where RPBE was used[52]. For Ru, this correction is 0.14 eV and for Pt the correction is 0.18 eV[66]. The values were added to all the corresponding PBE-calculated energies. Hydrogen adsorption energies can then be used to estimate the additive inverse of the overpotential ($-\eta_{HER}$), typically used as a metric of the electrocatalytic activity within the HER and defined as follows: $-\eta_{HER} = -\max(\Delta G_1, \Delta G_2)/e^- - U^o$, where $U^o = -0.83\, V$, $\Delta G_1 = \Delta G_H^{alkaline}$, $\Delta G_2 = \Delta G^o - \Delta G_1$, and $\Delta G^o = -2U^o = 1.66$ eV.

Table S6 compiles all the calculated free energies of adsorption for pure Ru surfaces and the respective $-\eta_{HER}$ while Table S7 shows the adsorption energies, their average, standard deviation, and the respective $-\eta_{HER}$ for the Ru NPs supported on TiN(100). In both tables, the coordination number (cn) of the adsorption site is also shown.

We also evaluated the energetics of the water dissociation reaction (ΔG_{S13}, see Eq. 14), on Ru(0001), Pt(111) and the most active site on Ru/TiN clusters (cn = 8). The results in Table S8 confirm that water dissociation is facilitated on pure Ru(0001) and TiN-supported Ru in comparison to Pt(111). Furthermore, the weaker adsorption of *H on Ru/TiN with respect to Ru(0001) accounts for its enhanced catalytic activity (Fig. 4b in the main text).

$$*H_2O + e^- + * \rightarrow *H + *OH \quad (14)$$

Note that *H was relaxed on the support, and we did not find favorable adsorption energies (1.56 eV), see the red data point in Fig. 4b. Hence, neither Ti nor N atoms of the TiN(001) support should be active for the HER. Although at first our hydrogen adsorption energies on TiN(100) (1.56 eV) differ significantly from those reported by Siodmiak et al. (−2.2 eV)[67], the differences stem from the use of different scales. Presumably, Siodmiak et al. carried out spin-restricted calculations using the H atom as a reference. Under such conditions, we get a binding energy of −1.83 eV, which is in line with the aforementioned value of −2.2 eV. For completeness, we performed spin-unrestricted adsorption calculations using the H atom as a reference,

obtaining a binding energy of −3.00 eV. This value is aligned with the results reported by Marlo and Milman using RPBE (−2.88 eV) and PW91 (−2.99 eV)[68]. The differences between our calculated energies and those in other studies probably stem from the use of different xc-functionals, DFT codes, convergence criteria, and spin effects. Anyway, under alkaline electrochemical conditions the H atom is not a suitable reference. Instead, we used H_2O as a reference to estimate the weak *H adsorption energy on TiN(100) of 1.56 eV.

Electronic-structure descriptors

From the values in Tables S6 and S7, linear trends between $\Delta G_H^{alkaline}$ and the coordination number of supported and pure Ru can be established, as shown in Fig. 4b in the main text. Here we show that the adsorption energies also correlate with electronic descriptors, such as the *d*-band center (ε_d) and the crystal orbital population integrated to the Fermi level (iCOOP). These electronic descriptors were calculated for the systems on which the most stable hydrogen adsorption was obtained (each of them having an adsorption site with a specific *cn*) using the post-processing VASPKIT[69] and the local-orbital basis suite towards electronic-structure reconstruction (LOBSTER) packages[70–73]. For comparison, Supplementary Fig. S30 presents the trends between the most stable adsorption energies for each *cn*.

Supplementary Fig. S31a shows the relationship between ΔG_H and ε_d of the Ru NPs. The latter was calculated by including all the Ru atoms in the nanoparticles. Supplementary Fig. S31b depicts ΔG_H the iCOOP of each Ru NP. For both descriptors, the Fermi level is used as reference (i.e., E_f = 0 eV).

Supplementary Figure S31a outlines a relationship between the *d*-band center of each supported Ru NP and ΔG_H. This linear trend suggests that *d*-band centers close to the Fermi level favor hydrogen adsorption when compared to largely negative values. This is in accordance with the *d*-band model of Hammer and Nørskov[74,75], which states that adsorption energies weaken because left-shifted *d*-bands promote the occupation of antibonding states.

The use of iCOOP as a descriptor in Supplementary Fig. S31b leads to similar trends. In a nutshell, positive COOP values indicate an overlap of bonding interactions between the adsorbate and the metal. Analogously, negative COOP values are correlated with antibonding interactions. Thus, positive integrated COOP values (iCOOP) suggest stronger bonding with more stable adsorption energies. Similar trends have been obtained when several atoms are adsorbed on transition metals[46] and when *H is adsorbed on metal-doped MoS_2[51].

Supplementary Figure S32 shows the correlation between the two electronic descriptors in Supplementary Figure S31. The correlation coefficient in this trend (r = 0.82) implies that the descriptors behave similarly in all of the Ru NPs examined and provide similar conclusions. In other words, they could be used interchangeably. This is supported by the similarity of the MAE/MAX in Figure S31 (MAE: 0.13 vs 0.16 eV; MAX: 0.34 vs 0.38 eV).

We performed analogous calculations for two extended surfaces of pure Ru, namely Ru(105) and Ru(109). Figure S33a-b show the trends for ΔG_H versus ε_d and iCOOP, respectively. ε_d for the extended Ru surfaces was calculated only considering the atoms involved in the adsorption. Similar to the Ru NPs, Ru(105) and Ru(109) display trends with negative slopes for both descriptors. However, the predictive capabilities of the electronic descriptors improve for the extended surfaces when compared to the Ru NPs. Specifically, Ru(109) and Ru(105) surfaces display MAE and MAX close to chemical accuracy (~0.04 eV) in all cases, while the supported Ru NPs involve MAE and MAX of ~0.14 eV and 0.36 eV in all cases. Although the two descriptors performed similarly, the *d*-band center yields the lowest MAE and MAX for both surfaces. Again, the correlation between both descriptors is strong (Supplementary Fig. S33c), suggesting that they could be used interchangeably, as observed for Ru NPs in Supplementary Fig. S32.

Furthermore, we combined the individual trends of Ru(105) and Ru(109) to obtain a single trend for pure Ru. To do so, we used the average values of the electronic descriptors when the *cn* of the Ru adsorption sites coincided, as done in Fig. 4b. The standard deviations were used as error bars for both descriptors. The trends for pure Ru are shown in Supplementary Fig. S34. The values used to build the trends in Supplementary Figs S30–S34 are compiled in Supplementary Table S9.

Kinetic volcano plot

The energies in Tables S6 and S7 were used to calculate the negative of the overpotential ($-\eta_{HER}$), used as an activity metric in Fig. 4c. We also elaborated a volcano using the model proposed by Nørskov et al.[52]. In their microkinetic model, the expressions for the HER exchange current density (i_o) depend on the strength of hydrogen adsorption. For weak adsorption, i.e., on the right leg of the volcano, the exchange current is:

$$i_o = \frac{-e_c \cdot k_0 \cdot e^{-\eta_{HER}/k_B T}}{1 + e^{-\eta_{HER}/k_B T}} \tag{15}$$

For strong adsorption, on the left leg of the volcano, the exchange current is:

$$i_o = \frac{-e_c \cdot k_0}{1 + e^{\eta_{HER}/k_B T}} \tag{16}$$

where η_{HER} is the overpotential, e_c is the charge of the electron ($1.602 \cdot 10^{-19}\ C$), k_B is the Boltzmann constant ($8.617 \cdot 10^{-5} eVK^{-1}$), T = 298.15 K, and k_0, the only free parameter, is the rate constant. The latter was adjusted using an experimental exchange current density of $-1.034\ mAcm^{-2}$. All the data used to build the volcano plot are presented in Table S10.

NP stability

We calculated the energy per atom of a Ru NP supported on TiN(100) as a means to assess its stability as:

$$Energy\ per\ Ru\ atom\ in\ the\ NP = \frac{E^{DFT}_{NP+TiN(100)} - E^{DFT}_{TiN(100)} - n \cdot E^{DFT}_{Ru\ ref.}}{n} \tag{17}$$

where $E^{DFT}_{NP+TiN(100)}$ is the DFT-calculated energy of the Ru NP supported on TiN(100), $E^{DFT}_{TiN(100)}$ is the DFT energy of TiN(100) without the Ru NP, $E^{DFT}_{Ru\ ref}$ is the energy of a Ru atom in a reference state, and n is the number of Ru atoms in the NP. For this analysis, we chose two reference states to obtain $E^{DFT}_{Ru\ ref.}$: one Ru atom in the gas phase and the energy of one Ru atom in an hcp bulk. Supplementary Fig. S35 shows the trends in the energy per Ru atom for several Ru NP of increasing size for both references. Supplementary Fig. S35 shows that for nanoparticles with ~10 Ru atoms or more, the energy per Ru atom starts to converge to a certain value. Moreover, the gap of 6.62 eV between the trends corresponds to the DFT-calculated cohesive energy of Ru (E_{coh}), in line with the experimental value of 6.74 eV.

Besides, we calculated the DFT adhesion energies (E^{DFT}_{adh}) of a Ru_{17} nanoparticle on TiN(100) and graphene and used them as proxies for the Ru stability in the Ru/TiN and Ru/C systems. The DFT binding energies are calculated as follows:

$$E^{DFT}_{bind} = E^{DFT}_{Ru_{17}*} - E^{DFT}_{*} - E^{DFT}_{Ru_{17}} \tag{18}$$

where $E^{DFT}_{Ru_{17}*}$ is the energy of the Ru NP on the support, E^{DFT}_{*} is the energy of the clean support (either TiN(100) or graphene), and $E^{DFT}_{Ru_{17}}$ is

the energy of the Ru NP alone. While a full relaxation was carried out to obtain $E^{DFT}_{Ru_{17}*}$ (the composite system: Ru_{17} + support), single-point calculations were performed to obtain E^{DFT}_{*} (support) and $E^{DFT}_{Ru_{17}}$ (nanoparticle) using the respective relaxed geometries yielded by the $E^{DFT}_{Ru_{17}*}$ calculation.

The values obtained from Eq. 18 are total adhesion energies ($\Delta E_{adh,tot}$), not adhesion energies per atom ($\Delta E_{adh,atom}$). To obtain the latter, $\Delta E_{adh,tot}$ is divided by the number of Ru atoms bound to the surface. For Ru_{17}, the number of Ru atoms in contact with TiN(100) and graphene is 7 in both cases, resulting in $\Delta E_{adh,atom}$ of −2.92 and −0.43 eV/atom, respectively. We also calculated a Ru_{21} cluster on TiN(100), which yielded a $\Delta E_{adh,atom}$ of −2.62 eV/atom, close to that of Ru_{17}. To assess the impact of graphene defects on the adhesion of Ru NPs, we calculated Ru_{17} bound to graphene with one and two C vacancies (monovacant and divacant graphene). The defects were created by removing C atoms initially in contact with Ru, which decreased the number of Ru atoms bound to graphene from 7 to 6. The resulting total and per-atom adhesion energies are in Supplementary Table S11 and Supplementary Fig. S36. C vacancies enhance the adhesion of the Ru cluster on graphene, changing $\Delta E_{adh,tot}$ from −2.99 to −9.05 eV ($\Delta E_{adh,atom}$ from −0.43 to −1.52 eV/atom) with one C vacancy, and from −9.05 to −13.53 eV (−1.51 to −2.25 eV/atom) with a second vacancy. This suggests that the adhesion energy of a given Ru cluster on graphene may only approach that on TiN(100) (−2.92 eV/atom) when numerous defects are created.

Data availability

The datasets generated during and/or analyzed during the current study are available in the figshare repository, https://doi.org/10.6084/m9.figshare.26233358.

References

1. Wang, H. et al. Strong metal–support interactions on gold nanoparticle catalysts achieved through Le Chatelier's principle. *Nat. Catal.* **4**, 418–424 (2021).
2. Parastaev, A. et al. Boosting CO_2 hydrogenation via size-dependent metal–support interactions in cobalt/ceria-based catalysts. *Nat. Catal.* **3**, 526–533 (2020).
3. Zhou, J. et al. Interfacial compatibility critically controls Ru/TiO_2 metal-support interaction modes in CO_2 hydrogenation. *Nat. Commun.* **13**, 327 (2022).
4. Zhang, J., Zhu, D., Yan, J. & Wang, C.-A. Strong metal-support interactions induced by an ultrafast laser. *Nat. Commun.* **12**, 6665 (2021).
5. Wu, P. et al. Harnessing strong metal–support interactions via a reverse route. *Nat. Commun.* **11**, 3042 (2020).
6. Kwak, N. W. et al. In situ synthesis of supported metal nanocatalysts through heterogeneous doping. *Nat. Commun.* **9**, 4829 (2018).
7. Zhang, J. et al. Strong metal–support interaction boosts activity, selectivity, and stability in electrosynthesis of H_2O_2. *J. Am. Chem. Soc.* **144**, 2255–2263 (2022).
8. Luo, Z., Zhao, G., Pan, H. & Sun, W. Strong metal–support interaction in heterogeneous catalysts. *Adv. Energy Mater.* **12**, 2201395 (2022).
9. Jiang, Z. et al. Lattice strain and schottky junction dual regulation boosts ultrafine ruthenium nanoparticles anchored on a N-Modified carbon catalyst for H_2 production. *J. Am. Chem. Soc.* **144**, 19619–19626 (2022).
10. Luo, T. et al. Fullerene lattice-confined Ru nanoparticles and single atoms synergistically boost electrocatalytic hydrogen evolution reaction. *Adv. Funct. Mater.* **33**, 2213058 (2023).
11. Zhou, S., Jang, H. & Qin, Q. Boosting hydrogen evolution reaction by phase engineering and phosphorus doping on Ru/P-TiO_2. *Angew. Chem. Int. Ed.* **21**, e202212196 (2022).
12. Gao, J. et al. Solar Water splitting with perovskite/silicon tandem cell and TiC-supported Pt nanocluster electrocatalyst. *Joule* **3**, 2930–2941 (2019).
13. Zuo, Y. et al. Ru–Cu Nanoheterostructures for efficient hydrogen evolution reaction in alkaline water electrolyzers. *J. Am. Chem. Soc.* **145**, 21419–21431 (2023).
14. Wu, Y. L. et al. Ordered Macroporous superstructure of nitrogen-doped nanoporous carbon implanted with ultrafine Ru nanoclusters for efficient pH-universal hydrogen evolution reaction. *Adv. Mater.* **33**, 2006965 (2021).
15. Tung, C. W. et al. Dynamic Co(μ-O)$_2$Ru moiety endowed efficiently catalytic hydrogen evolution. *Adv. Energy Mater.* **12**, 2200079 (2022).
16. Wang, K. et al. Kinetically accelerating elementary steps via bridged Ru-H state for the hydrogen-evolution in anion-exchange membrane electrolyzer. *Adv. Funct. Mater.* **33**, 2212321 (2023).
17. Zhang, H., Zhou, W., Lu, X. F., Chen, T. & Lou, X. W. Implanting isolated Ru atoms into edge-rich carbon matrix for efficient electrocatalytic hydrogen evolution. *Adv. Energy Mater.* **10**, 2000882 (2020).
18. Liang, Q. et al. Superassembly of surface-enriched Ru nanoclusters from trapping–bonding strategy for efficient hydrogen evolution. *ACS Nano* **16**, 7993–8004 (2022).
19. Lao, M. et al. Manipulating the coordination chemistry of RuN(O)C moieties for fast alkaline hydrogen evolution kinetics. *Adv. Funct. Mater.* **31**, 2100698 (2021).
20. Zhang, M. et al. Ru-RuO_2/CNT hybrids as high-activity pH-universal electrocatalysts for water splitting within 0.73 V in an asymmetric-electrolyte electrolyzer. *Nano Energy* **61**, 576–583 (2019).
21. Chen, L.-N. et al. Ru nanoparticles supported on partially reduced TiO_2 as highly efficient catalyst for hydrogen evolution. *Nano Energy* **88**, 106211 (2021).
22. Kim, E.-J. et al. Stabilizing role of Mo in TiO_2-MoO_x supported Ir catalyst toward oxygen evolution reaction. *Appl. Catal. B Environ.* **280**, 119433 (2021).
23. Nong, S. et al. Well-dispersed ruthenium in mesoporous crystal TiO_2 as an advanced electrocatalyst for hydrogen evolution reaction. *J. Am. Chem. Soc.* **140**, 5719–5727 (2018).
24. Li, J. et al. Boosting electrocatalytic activity of Ru for acidic hydrogen evolution through hydrogen spillover strategy. *ACS Energy Lett.* **7**, 1330–1337 (2022).
25. Chen, D. et al. Ultralow Ru loading Transition metal phosphides as high-efficient bifunctional electrocatalyst for a solar-to-hydrogen generation system. *Adv. Energy Mater.* **10**, 2000814 (2020).
26. Wang, D., Li, Q., Han, C., Xing, Z. & Yang, X. Single-atom ruthenium based catalyst for enhanced hydrogen evolution. *Appl. Catal. B Environ.* **249**, 91–97 (2019).
27. Luo, Z. et al. Reactant friendly hydrogen evolution interface based on di-anionic MoS_2 surface. *Nat. Commun.* **11**, 1116 (2020).
28. Sun, Y. et al. Modulating electronic structure of metal-organic frameworks by introducing atomically dispersed Ru for efficient hydrogen evolution. *Nat. Commun.* **12**, 1369 (2021).
29. Li, G. et al. The synergistic effect of Hf-O-Ru bonds and oxygen vacancies in Ru/HfO_2 for enhanced hydrogen evolution. *Nat. Commun.* **13**, 1270 (2022).
30. van Deelen, T. W., Hernández Mejía, C. & de Jong, K. P. Control of metal-support interactions in heterogeneous catalysts to enhance activity and selectivity. *Nat. Catal.* **2**, 955–970 (2019).
31. Zhang, L.-N. et al. Cable-like Ru/WNO@C nanowires for simultaneous high-efficiency hydrogen evolution and low-energy consumption chlor-alkali electrolysis. *Energy Environ. Sci.* **12**, 2569–2580 (2019).
32. Xu, J. et al. Boosting the hydrogen evolution performance of ruthenium clusters through synergistic coupling with cobalt phosphide. *Energy Environ. Sci.* **11**, 1819–1827 (2018).
33. Tu, K. et al. A novel heterostructure based on RuMo nanoalloys and N-doped carbon as an efficient electrocatalyst for the hydrogen evolution reaction. *Adv. Mater.* **32**, 2005433 (2020).

34. Avasarala, B. & Haldar, P. Durability and degradation mechanism of titanium nitride based electrocatalysts for PEM (proton exchange membrane) fuel cell applications. *Energy* **57**, 545–553 (2013).
35. Liu, Y.-R., Hsueh, Y.-C. & Perng, T.-P. Fabrication of TiN inverse opal structure and Pt nanoparticles by atomic layer deposition for proton exchange membrane fuel cell. *Int. J. Hydrog. Energy* **42**, 10175–10183 (2017).
36. Liu, F., Yang, X., Dang, D. & Tian, X. Engineering of hierarchical and three-dimensional architectures constructed by titanium nitride nanowire assemblies for efficient electrocatalysis. *ChemElectroChem*. **6**, 2208–2214 (2019).
37. Patel, P. P. et al. High performance and durable nanostructured TiN supported Pt_{50}–Ru_{50} anode catalyst for direct methanol fuel cell (DMFC). *J. Power Sources* **293**, 437–446 (2015).
38. Wang, C. et al. Quasi-atomic-scale platinum anchored on porous titanium nitride nanorod arrays for highly efficient hydrogen evolution. *Electrochim. Acta* **292**, 727–735 (2018).
39. Anandhababu, G., Babu, D. D., Manimuthu, V. & Baskaran, S. Profuse surface activation of Ir-dispersed titanium nitride bifunctional electrocatalysts. *Adv. Energy Sustainability Res* **2**, 2000054 (2021). **2021**.
40. Yang, S., Kim, J., Tak, Y. J., Soon, A. & Lee, H. Single-Atom catalyst of platinum supported on titanium nitride for selective electrochemical reactions. *Angew. Chem. Int. Ed.* **55**, 2058–2062 (2015).
41. Kim, J. et al. Tailoring Binding Abilities by incorporating oxophilic transition metals on 3D nanostructured Ni arrays for accelerated alkaline hydrogen evolution reaction. *J. Am. Chem. Soc.* **143**, 1399–1408 (2020).
42. Qi, H. et al. Highly selective and robust single-atom catalyst Ru1/NC for reductive amination of aldehydes/ketones. *Nat. Commun.* **12**, 3295 (2021).
43. Radinger, H., Trouillet, V., Bauer, F. & Scheiba, F. Work function describes the electrocatalytic activity of graphite for vanadium oxidation. *ACS Catal.* **12**, 6007–6015 (2022).
44. Li, J. et al. A fundamental viewpoint on the hydrogen spillover phenomenon of electrocatalytic hydrogen evolution. *Nat. Commun.* **12**, 3502 (2021).
45. Nandan, R. et al. Atomic arrangement modulation in CoFe nanoparticles encapsulated in N-doped carbon nanostructures for efficient oxygen reduction reaction. *ACS Appl. Mater.* **13**, 3771–3781 (2021).
46. Su, H. Y. et al. Establishing and understanding adsorption-energy scaling relations with negative slopes. *J. Phys. Chem. Lett.* **7**, 5302–5306 (2016).
47. Anantharaj, S., Noda, S., Driess, M. & Menezes, P. W. The pitfalls of using potentiodynamic polarization curves for tafel analysis in electrocatalytic water splitting. *ACS Energy Lett.* **6**, 1607–1611 (2021).
48. Calle-Vallejo, F. The ABC of generalized coordination numbers and their use as a Descriptor in electrocatalysis. *Adv. Sci.* **10**, 2207644 (2023).
49. Calle-Vallejo, F., Martínez, J. I., García-Lastra, J. M., Sautet, P. & Loffreda, D. Fast prediction of adsorption properties for platinum nanocatalysts with generalized coordination numbers. *Angew. Chem. Int. Ed.* **53**, 8316–8319 (2014).
50. Jiang, T. et al. Trends in CO oxidation rates for metal nanoparticles and close-packed, stepped, and kinked surfaces. *J. Phys. Chem. C.* **113**, 10548–10553 (2009).
51. Su, H. Y., Ma, X. & Sun, K. Single-atom metal tuned sulfur vacancy for efficient H_2 activation and hydrogen evolution reaction on MoS_2 basal plane. *Appl. Surf. Sci.* **597**, 153614 (2022).
52. Nørskov, J. K. et al. Trends in the exchange current for hydrogen evolution. *J. Electrochem. Soc.* **152**, J23 (2005).
53. Zhao, J., Liao, N. & Luo, J. Transforming NiFe layered double hydroxide into $NiFeP_x$ for efficient alkaline water splitting. *J. Mater. Chem. A* **11**, 9682–9690 (2023).
54. Zuo, Y. et al. High-performance alkaline water electrolyzers based on Ru-perturbed Cu nanoplatelets cathode. *Nat. Commun.* **14**, 4680 (2023).
55. Kresse, G. & Furthmüller, J. Efficient iterative schemes for ab initio total-energy calculations using a plane-wave basis set. *Phys. Rev. B* **54**, 11169–11186 (1996).
56. Kresse, G. & Joubert, D. From ultrasoft pseudopotentials to the projector augmented-wave method. *Phys. Rev. B* **59**, 1758–1775 (1999).
57. Perdew, J. P., Burke, K. & Ernzerhof, M. Generalized gradient approximation made simple. *Phys. Rev. Lett.* **77**, 3865–3868 (1996).
58. Methfessel, M. & Paxton, A. T. High-precision sampling for Brillouin-zone integration in metals. *Phys. Rev. B* **40**, 3616–3621 (1989).
59. Monkhorst, H. J. & Pack, J. D. Special points for Brillouin-zone integrations. *Phys. Rev. B* **13**, 5188–5192 (1976).
60. Rumble, J. (Ed.). *CRC Handbook Of Chemistry And Physics*. 104th edn, (CRC Press, 2023).
61. Nørskov, J. K. et al. Origin of the overpotential for oxygen reduction at a fuel-cell cathode. *J. Phys. Chem. B* **108**, 17886–17892 (2004).
62. Urrego-Ortiz, R., Builes, S. & Calle-Vallejo, F. Automated versus chemically intuitive deconvolution of density functional theory (DFT)-based gas-phase errors in nitrogen compounds. *Ind. Eng. Chem. Res.* **61**, 13375–13382 (2022).
63. Peterson, A. A., Abild-Pedersen, F., Studt, F., Osmiumsl, J. R. & Nørskov, J. K. How copper catalyzes the electroreduction of carbon dioxide into hydrocarbon fuels. *Energy Environ. Sci.* **3**, 1311–1315 (2010).
64. Saleheen, M. & Heyden, A. liquid phase modeling in heterogeneous catalysis. *ACS Catal.* **8**, 2188–2194 (2018).
65. Heenen, H. H., Gauthier, J. A., Kristoffersen, H. H., Ludwig, T. & Chan, K. Solvation at metal/water interfaces: an ab initio molecular dynamics benchmark of common computational approaches. *J. Chem. Phys.* **152**, 144703 (2020).
66. Pohl, M. D., Watzele, S., Calle-Vallejo, F. & Bandarenka, A. S. Nature of highly active electrocatalytic sites for the hydrogen evolution reaction at Pt electrodes in acidic media. *ACS omega* **2**, 8141–8147 (2017).
67. Siodmiak, M., Govind, N., Andzelm, J., Tanpipat, N. & Korkin, A. Theoretical study of hydrogen adsorption and diffusion on TiN(100) Surface. *Phys. Stat. Sol. B* **226**, 29–36 (2001).
68. Marlo, M. & Milman, V. Density-functional study of bulk and surface properties of titanium nitride using different exchange-correlation functionals. *Phys. Rev. B* **62**, 2899–2907 (2000).
69. Wang, V., Xu, N., Liu, J. C., Tang, G. & Geng, W. T. VASPKIT: A user-friendly interface facilitating high-throughput computing and analysis using VASP Code. *Comput. Phys. Commun.* **267**, 108033 (2019).
70. Deringer, V. L., Tchougréeff, A. L. & Dronskowski, R. Crystal orbital hamilton population (COHP) analysis as projected from plane-wave basis sets. *J. Phys. Chem. A* **115**, 5461–5466 (2011).
71. Maintz, S., Deringer, V. L., Tchougréeff, A. L. & Dronskowski, R. Analytic projection from plane-wave and PAW wavefunctions and application to chemical-bonding analysis in solids. *J. Comput. Chem.* **34**, 2557–2567 (2013).
72. Maintz, S., Deringer, V. L., Tchougréeff, A. L. & Dronskowski, R. LOBSTER: a tool to extract chemical bonding from plane-wave based DFT. *J. Comput. Chem.* **37**, 1030–1035 (2016).
73. Nelson, R., Ertural, C., George, J., Deringer, V. & Dronskowski, R. LOBSTER: local orbital projections, atomic charges, and chemical bonding analysis from projector-augmented-wave-based DFT. *J. Comput. Chem.* **41**, 1931–1940 (2020).
74. Hammer, B. & Nørskov, J. K. Electronic factors determining the reactivity of metal surfaces. *Surf. Sci.* **343**, 211–220 (1995).
75. Hammer, B. & Nørskov, J. K. Theoretical surface science and catalysis — calculations and concepts. *Adv. Catal.* **45**, 71–129 (2000).

Acknowledgements
The authors acknowledge the funding support from the National Key Research and Development Program of China (Grant No. 2021YFF0501900), the Excellent Young Scholar Fund from the National Science Foundation of China (Grant No. 22122903), the Tianjin Distinguished Young Scholar Fund (Grant No. 20JCJQJC00260), the"111"-Project (Grant No. B16027), a PhD fellowship from "la Caixa" Foundation (ID 100010434, fellowship code LCF/BQ/DI22/11940040), grants PID2021-127957NB-I00 and TED2021-132550BeC21 funded by MCIN/AEI/10.13039/501100011033 and the European Union, and grant IT1453-22 "Grupos Consolidados UPV/EHU del Gobierno Vasco". The authors acknowledge Dr Daniel Wun Fung Cheung for revising the English of the manuscript.

Author contributions
J.L. and J.Z. conceived the project. J.L. supervised the project. Federico Calle-Vallejo supervised the computational research. J.Z. carried out the experiments and analyzed the data. R.U.-O. performed the DFT calculations and modeling. N.L. performed the AEM water electrolyzer tests. All authors participated in the discussion of experimental and calculation results. The manuscript was written through the contributions of all authors. All authors have given approval to the final version of the manuscript.

Competing interests
J.Z. and J.L. declare the following competing interests: J.Z. and J.L. have filed a patent application regarding the catalysts in the manuscript. The other authors declare no competing interests.

Additional information
Supplementary information The online version contains supplementary material available at https://doi.org/10.1038/s41467-024-50691-5.

Correspondence and requests for materials should be addressed to Federico Calle-Vallejo or Jingshan Luo.

Peer review information *Nature Communications* thanks Chuan Xia and the other anonymous reviewer(s) for their contribution to the peer review of this work. A peer review file is available.